Title

A New Pulse Counting Low Energy Electron Diffraction (LEED) System Based on a Position Sensitive Detector

Journal

Review of scientific instruments, 63(1)

Authors

Ogletree, D.F.
Blackman, G.S.
Hwang, R.Q.
et al.

Publication Date

1991-09-01

LBL-30746
Preprint

Center for Advanced Materials

CAM

Submitted to the Review of Scientific Instruments

A New Pulse Counting Low Energy Electron Diffraction (LEED) System Based on a Position Sensitive Detector

D.F. Ogletree, G.S. Blackman, R.Q. Hwang, U. Starke,
J.E. Katz, and G.A. Somorjai

September 1991

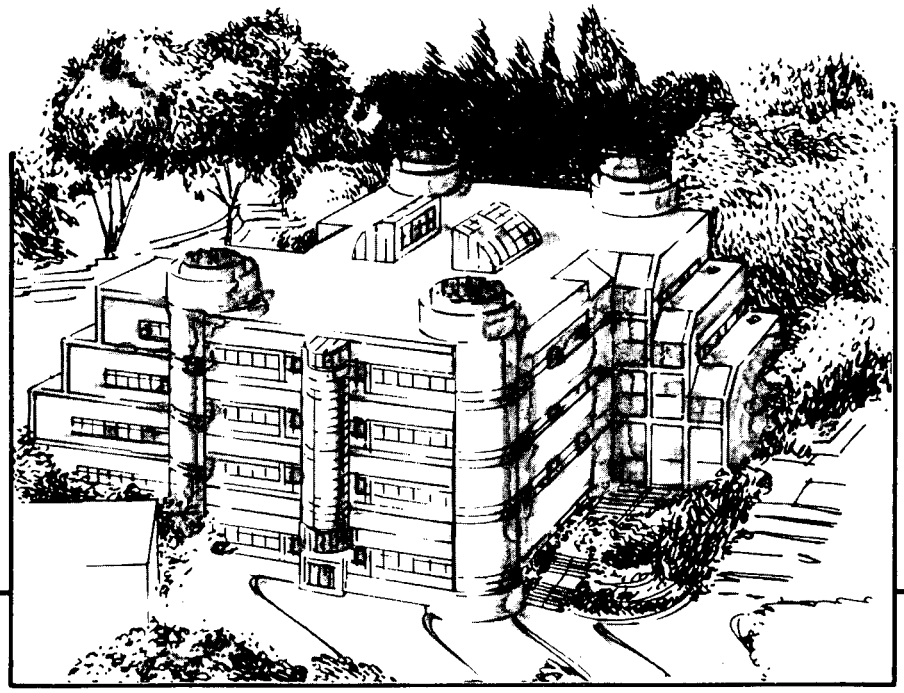

Materials and Chemical Sciences Division

Lawrence Berkeley Laboratory • University of California

ONE CYCLOTRON ROAD, BERKELEY, CA 94720 • (415) 486-4755

Prepared for the U.S. Department of Energy under Contract DE-AC03-76SF00098

DISCLAIMER

LBL-30746

A NEW PULSE COUNTING LOW ENERGY ELECTRON DIFFRACTION (LEED) SYSTEM BASED ON A POSITION SENSITIVE DETECTOR

D. Frank Ogletree, G.S. Blackman, R.Q. Hwang, U. Starke , J.E. Katz[1] and G.A. Somorjai

Materials Sciences Division
Center for Advanced Materials
Lawrence Berkeley Laboratory
University of California
Berkeley, CA 94720 U.S.A.

[1]Engineering Division
Lawrence Berkeley Laboratory
University of California
Berkeley, CA 94720 U.S.A.

ACKNOWLEDGMENT
This work was supported by the Director, Office of Energy Research, Office of Basic Energy Sciences, Material Sciences Division, U.S. Department of Energy under contract No. DE-AC03--76SF00098.

A New Pulse Counting Low Energy Electron Diffraction (LEED) System Based on a Position Sensitive Detector

D. Frank Ogletree, G. S. Blackman, R. Q. Hwang, U. Starke and G. A. Somorjai

Center for Advanced Materials
Materials Sciences Division

J. E. Katz

Engineering Division

Lawrence Berkeley Laboratory
1 Cyclotron Road
Berkeley, California 94720

ABSTRACT

A new Low Energy Electron Diffraction (LEED) system has been constructed with a pulse counting position sensitive detector using channel plates and a wedge and strip anode. The detector accepts diffracted electrons over a 120° angle and the LEED pattern is recorded as a 256 x 256 pixel image. Individual LEED spot intensities can be measured up to a maximum linear count rate of $\sim$ 5 KHz while the dark count rate is $\sim$ 0.02 Hz, yielding a dynamic range greater than 10^5. Incident beam currents for LEED measurements are $\sim$ 1 pA. Diffuse LEED intensities from disordered systems can be measured using the large dynamic range of this instrument. Examples of diffuse LEED measurements are presented. The low incident beam currents also allow for LEED I-V measurements on surfaces sensitive to electron beam damage and on non-conducting surfaces.

September 24, 1991

A New Pulse Counting Low Energy Electron Diffraction (LEED) System Based on a Position Sensitive Detector

D. Frank Ogletree, G. S. Blackman, R. Q. Hwang, U. Starke and G. A. Somorjai

Center for Advanced Materials
Materials Sciences Division

J. E. Katz

Engineering Division

Lawrence Berkeley Laboratory
1 Cyclotron Road
Berkeley, California 94720

1. Introduction

Low energy electron diffraction (LEED) is a powerful technique for surface structure determination. Over 550 clean surface and adsorbed monolayer structures have been analyzed by fitting experimental diffraction spot intensity versus energy (I-V) curves to theoretical I-V curves calculated for model structures. Using modern "dynamical" LEED theories adsorption sites and bond lengths can be obtained with an accuracy of 0.05 Å or better.[1,2,3]

There are three important classes of surface structures that have been generally inaccessible to LEED: surfaces or overlayers that are extremely sensitive to electron beam damage, systems which do not posses long range order, and non-conducting or poorly conducting surfaces which present charging problems. For LEED to be widely applied to these systems, instruments of increased sensitivity and dynamic range are required. In this paper we describe a new "digital" LEED system based on a position

sensitive pulse counting electron detector and a low current electron gun which meets these requirements.

1.1. Beam sensitive structures

Electron beam damage with conventional LEED systems can be so severe as to make structural analysis impractical for a number of significant surface systems. Ionic crystals interact strongly with low energy electrons and have a high damage rate. Hydrogen bonding is important in the structure of water overlayers, and these layers are easily disrupted by electron beams. Some organic compounds are relatively resistant to beam damage, such as ethylidyne adsorbed on transition metals like Pt(111) or Rh(111), while others like acetylene which has a C=C double bond parallel to the surface, are sensitive to beam damage when adsorbed on the same metal surfaces.

1.2. Diffuse LEED

Recent theoretical developments have extended LEED structure determination to certain classes of disordered systems. By making analogies to NEXAFS (near edge x-ray adsorption fine structure), Pendry[4] has developed a theory which allows the calculation of LEED intensities in non-Bragg directions for a single adsorbate molecule or point defect on an otherwise ordered substrate. This formalism can be applied to "lattice gas" systems, where adsorbate molecules are located in one or a few types of local geometries but without long range order on the surface.

Comparison of experimental "diffuse" LEED intensities with calculations for model structures can determine local binding geometries just as I-V (intensity-voltage) calculations are used for ordered structures. An extension of the "beam-set-neglect" theory used in LEED I-V calculations can significantly increase the efficiency of diffuse LEED calculations.[5,6] Several systems have been analyzed with diffuse LEED, including disordered oxygen on W(100),[7,8] oxygen and sulfur on Ni(100),[9,10] and disordered carbon monoxide on Pt(111)[11] and Ru(0001).[12] These experiments require sensitive measurements of the diffuse background intensities of LEED patterns, which are typically three orders of magnitude weaker than the diffracted Bragg beam intensities.

In the next section of this paper we review different types of LEED instrumentation and the third section describes our new LEED detector. Section four covers the position sensitive anode, including design and construction details. Section five describes the position calculation electronics and section six is an analysis of noise and performance. The final section outlines experimental data obtained with our new detector, including its application to diffuse LEED measurements.

2. LEED Instrumentation

Most commercial LEED instruments use a "display LEED" optics with a retarding field energy analyzer (RFA) followed by a phosphor screen. The quasi-elastically backscattered LEED electrons pass through the RFA grids and are accelerated into the phosphor screen at 5-10 KeV, producing a reciprocal space image of the diffraction pattern. Incident beam currents of ~ 1 μA produce LEED patterns bright enough to see with the

unaided eye.

One simple way to make LEED I-V measurements is to image the LEED screen with a video camera and digitize the image. The details of spot tracking, background subtraction and calculations of integrated spot intensities can then be handled in software.[13,14] Using a standard RS-170 vidicon camera and 8-bit video frame grabber LEED I-V measurements have an effective dynamic range of $\sim 10^2$. The sensitivity is limited by the relatively high dark currents of vidicon tubes and the difficulty of increasing the incident electron beam current beyond a few μA at typical LEED energies of $\sim$ 100 eV. More recently slow scan frame transfer CCD (charge coupled device) cameras with digital readouts have become commercially available. This type of camera can increase the dynamic range and sensitivity by at least an order of magnitude over the vidicon camera.[15]

Further increases in sensitivity can be obtained using image intensified video cameras. In these systems the light from the LEED screen falls on a photo-cathode, and the emitted electrons are amplified using one or more channel plate electron multipliers. The amplified electron image hits a phosphor target, emitting an amplified light image which can be recorded with a video camera.[16] Image gains of 10^2 to 10^7 can be obtained at the cost of increased noise and reduced dynamic range. The image is degraded by four consecutive electron-photon conversions. Furthermore, channel plates are rather noisy when used as analog amplifiers since the output pulse height distribution has a substantial spread, several times the average pulse height.[17]

Instead of using an image intensified camera, we have chosen to build the channel plates into our LEED detector to directly amplify the electron diffraction pattern. With a chevron arrangement of two or more channel plates gains of 10^6 to 10^7 can be obtained, which is sufficient for pulse counting of electron events. A position sensitive anode is used to make an analog calculation of the spatial position of each discrete electron event. With this arrangement, the sensitivity and dynamic range of the LEED detector are limited only by shot noise in the diffraction pattern, the detector dark count rate, and the onset of gain saturation of the channel plate amplifier. Channel plate gain fluctuations and electronic noise do not effect the measurement of LEED intensities, although they do limit the detector spatial resolution.

Although we have concentrated on LEED experiments, this detector could easily be used in other experiments where angle-resolved detection of low energy charged particles is needed. Possible applications include photoelectron diffraction, angle resolved Auger, x-ray or ultra-violet photoemission (XPS and UPS) spectroscopy and electron or photon stimulated ion desorption angular distributions (ESDIAD).

3. LEED Detector Design

A block diagram of the digital LEED detector is shown in figure 1. The overall layout is similar to a conventional LEED optics, using a retarding field energy analyzer with a co-axial electron gun, where the phosphor screen is replaced by a pair of channel plates and a position sensitive anode. The detector is enclosed in magnetic shielding, and a second layer of magnetic shielding encloses the electron gun. The detector is less sensitive to external magnetic fields than a conventional display LEED optics.

3.1. Energy analyzer

The sample is placed at the focus of a retarding field energy analyzer formed from three concentric grids with an average radius of $\sim$ 40 mm.[18] The sample and the first grid are grounded, forming a field free region around the sample. The second and third grids are biased a few volts positive with respect to the incident electron energy V_{beam}, so only the quasi-elastically scattered electrons can pass through the biased grids.

The front face of the input channel plate is biased at $\sim V_{beam} + 700$ volts. Electrons passing through the biased grids are accelerated into the channel plates and impact with an energy independent of V_{beam}. The 700 volt bias creates an electric field between the last grid and the channel plate that projects the LEED electrons along trajectories approximately perpendicular to the channel plates. This has two beneficial effects -- first, all electrons strike the channel plates at near normal incidence, so the variations in quantum efficiency across the channel plates are minimized, and second, as with a hemispherical phosphor screen, the pattern on the detector represents a linear projection of reciprocal space. The measured reciprocal space distortion is less than 2% across the image.

3.2. Channel plates

Image amplifiers and position-sensitive electron detectors are used for a wide range of applications. All of these instruments use channel plates (channel electron multiplier arrays or microchannel plates) as electron amplifiers.

Channel plates are sensitive to photons above $\sim$ 10 eV and to charged particles. A single incident low-energy electron (100 to 1000 eV) can trigger a charge-pulse with a

quantum efficiency of over 50%.[17,19,20,21,22] The gain of a channel is limited by ion-feedback, caused by ions traveling back up the channels. This is commonly prevented by stacking two channel plates in a "chevron" array, where the channels in the two plates are aligned a few degrees off normal. Electrons change direction to follow the channels more easily than ions, so high electron gain is possible while ion feedback is suppressed. The gain of a pair of channel plates in a chevron arrangement can exceed $5 \cdot 10^7$. Background or dark-count rates below 1 Hz/cm^2 are commonly obtained for channel plates in a chevron array.[17,19]

The spatial resolution of channel plate detectors is ultimately limited by the channel size. In a chevron stack one excited channel in the input plate triggers several channels in the output plate, which degrades the spatial resolution for analog imaging applications. When channel plates are operated in a saturated-gain pulse-counting mode there is a relatively wide output pulse height distribution, $\sim$ 50 to 150% of the mean pulse height. The gain fluctuations can be even greater in the analog mode.

The LEED detector uses a pair of high bias current (30 μA) 75 mm channel plates with 25 μm channels on 32 μm centers. The channels have an 8° bias angle, and the channel plates have a 6 mm hole in the center for the LEED electron gun. Each channel plate is biased at 1000 to 1200 V in order to operate in the saturated gain mode.

3.3. Electron gun

A commercial electron gun of conventional design is used with the LEED detector.[23] Emission from a thoriated iridium filament is controlled by an extractor (Wehnelt) electrode and collected at the first anode. A 37 μm beam aperture is attached to the

first anode at the cross-over position of the beam, and a three element Einzel lens then images the beam onto the detector. The first anode voltage is held constant at ~ 400 V independent of the beam voltage in order to maintain a constant beam current. The beam is accelerated or decelerated as it passes through the focusing lens and the incident beam voltage can be varied from ~ 5 to 1000 volts. Typical beam currents for LEED experiments are 1 to 10 pA.

The electron gun beam tube at ground potential passes through the anode and channel plates at $\sim +2.5$ kV. This produces a strong electrostatic field which distorts the charge cloud diffusion between the channel plates and the anode, so an electrostatic shield is wrapped around the beam tube and biased to a voltage intermediate between the anode and the output side of the channel plate. The exact bias voltage does not seem to effect the anode performance provided $V_{output} \leq V_{bias} \leq V_{anode}$.

4. Position Sensitive Detection

Detectors using channel plates with position-sensitive anodes have been used for many applications, including space-borne EUV telescopes,[24,25] x-ray spectrometers,[21] dispersive electron spectrometers[26] and LEED.[27,28] A number of different position sensitive charge collection schemes have been developed, including multi-anode schemes, coincidence detection and charge division, depending on the resolution and counting rates required.[29,26]

4.1. Charge division

The digital LEED detector uses a charge-division anode. In this scheme the charge cloud produced by a single channel plate pulse falls on the anode which is connected to three or four charge sensitive amplifiers. The ratios of the charge collected by the different amplifiers is a linear function of position. This approach has two important advantages -- first, since the calculation of the position of an event depends only on charge ratios, channel plate gain fluctuations do not have a direct affect on the detector performance. Second, since charge division is a linear function of position, the anode detects the centroid of the charge distribution, so charge spreading caused by multiple channel excitation in the second channel plate of a chevron array does not degrade the spatial resolution for charge-clouds with radial symmetry, unlike in optical imaging systems.

One disadvantage of charge division is pulse pile-up. To avoid position errors, the charge from one event must dissipate and the amplifiers must return to baseline before the next event takes place. This requires a count rate that is slow compared to the detector time constant.

4.2. Resistive anode

The first two dimensional charge-division scheme used a resistive anode.[30] Charge sensitive amplifiers are connected to each corner of a square thick-film resistor on a ceramic substrate which is placed on the output side of the channel plates. When this resistor is terminated with line-resistors along circular arcs, the charge collected at each corner is a linear function of position.[31] The resistive anode was used by Stair[27] in the

first position sensitive LEED detector and also by McRae.[28] Similar detectors are now available commercially.[32] A resistive anode was also used in the first version of our digital LEED detector. With this anode total count rates up to $5 \cdot 10^3$ with 100x100 resolution are possible for a detector using 75 mm channel plates.

The speed of the resistive anode is determined by its RC time constant. For the 75 mm detector the parasitic capacitance was $\sim$ 100 pF and the anode resistance was $\sim$ 10 KΩ/square for a time constant of ~ 1 μs. The resulting pulse pair resolution was ~ 8 μs (i.e. the minimum time separating valid events). This is longer than the time constant because the amplifiers must return to the baseline between events for accurate position calculation.

The main disadvantage of the resistive anode is that detector performance is limited by the anode properties. Resistive anodes work quite well for 25 mm channel plates, however, for 75 mm plates the time constant is nine times longer due to the increased capacitance. The resistance cannot be reduced in proportion because the input noise of a charge-sensitive amplifier is proportional to $R_{in}^{-1/2}$. Reducing the anode resistance increases electrical noise and degrades the spatial resolution.

The linearity of the resistive anode position determination is controlled by the uniformity of the resistive film and the accuracy of the resistive edge termination. In practice the deviations from linearity are $\sim 5\%$ across the anode. The resolution is limited by the electrical noise of the amplifiers and thermal noise in the resistor.

4.3. Wedge and strip anode

The final version of the LEED detector uses a different type of position sensitive anode, the "wedge-and-strip" design invented by H. O. Anger.[24,33] This anode involves three metal conductors in an interlocking pattern with a spatial period $\sim$ 1 mm (figure 2). The anode is separated from the channel plate by several millimeters so the output charge cloud spreads out over a few anode periods. The relative area of each conductor in the area of the charge "foot print" is a linear function of position.

The anode has three electrodes, the wedges A, the strips B and the remaining area between the wedges and strips C. If a charge cloud lands on the left side of the anode, over the narrow strips, the collected charge Q_B is small and if it lands on the right side, where the strips are wide, Q_B is larger. Likewise, if the charge cloud lands near the bottom of the anode, near the peak of the wedges, Q_A is small and if it lands near the top of the anode, at the base of the wedges, Q_A is larger. The event coordinates are proportional to

$$x \approx \frac{Q_B}{Q_A + Q_B + Q_C} \quad \text{and} \quad y \approx \frac{Q_A}{Q_A + Q_B + Q_C} \tag{1}$$

The actual coordinates are scaled depending on the ratio of the maximum and minimum widths of the strips and wedges.

The performance of the wedge-and-strip anode system is limited by the channel plate performance. Wedge-and-strip anodes can be fabricated by photo-lithography to any desired degree of accuracy, so linearity is not a problem. If two charge pulses arrive at the anode in a time shorter than the processing time the resulting position calculations will be in error. The RC time constant of the anode and signal cables is $\sim$ 10 ns,

so the anode can support count rates up to 50 MHz. The wedge-and-strip anode is also better able to discriminate against pulse pile-up. It is much easier to distinguish coincidence events with the $\sim$ 50 ns rise time of a metal wedge-and-strip anode preamp than with the $\sim$ 1 μs rise time of the resistive anode amplifiers.

Several factors need to be balanced in an optimum anode design. Electrode capacitance should be minimized to reduce preamp noise and input impedance, which also reduces inter-electrode capacitive coupling. The range of wedge and strip widths should be large to maximize the variation in the fraction of charge collected by one electrode $(f_{\max} - f_{min})$. The anode period width needs to be small enough so that the charge cloud footprint settling on the anode covers several periods, otherwise interference or "aliasing" effects can cause position errors.

Each anode period has four insulating gaps to separate the A, B and C electrodes. Small gaps increase the inter-electrode capacitance and the complexity of fabrication while reducing the "dead" or non-conducting area of the anode. Reducing the anode period width requires more periods across the anode, decreasing the total conductive area and increasing the electrode perimeter and inter-electrode capacitance. We chose a period of 1500 μm and a gap of 44 μm for a 12% dead area due to insulating gaps. The final anode pattern is shown in figure 3.

4.4. Anode fabrication

The wedge and strip anode was produced by photo-lithography. A quartz glass substrate was chosen for its stability and low dielectric constant. The surface was coated with 5 microns of copper and coated with photo-resist and then baked at 150° C. A mask was positioned on the substrate and exposed to UV light for 30 s. After exposure, the anode was developed and the copper was etched in a ferric chloride solution for about 100 s.

The wedge-and-strip position sensitive anode is mounted $\sim$ 6 mm behind the output side of the channel plates to allow the output charge pulse room to spread. The anode is biased by +75 to +600 V positive relative to the output side of the channel plates. The exact bias voltage has only a slight influence on the spatial resolution of the anode.

5. Position Calculation Electronics

The digitizer electronics convert the charges collected on the wedge and strip anode during an electron event into (x,y) coordinates. The incident charges Q_A, Q_B and Q_C are digitized individually and the position calculation algorithm is implemented in dedicated digital logic.

The analog front end of the LEED position digitizer consists of an integrating charge sensitive preamplifier for each of the three anode electrodes. This is followed by analog circuitry operating in the derivative mode producing shaped pulses whose height is proportional to the charge deposited on the electrode.

The three pre-amp signals are summed and fed to a fourth shaping amplifier with a peak detection circuit that triggers three separate 12-bit flash analog to digital converters (Burr Brown 803-CM) which digitize the A, B and C pulse heights with a conversion time of 750 ns. The full height of each shaped pulse is proportional to the change deposited on the corresponding electrode. The average charge per incident electron is 6.5 pC, or a gain of $\sim 4 \cdot 10^7$. A discriminator rejects events if the total collected charge is $<$ 1pC (excessive error in position determination) or $>$ 10 pC (possible pulse pile-up or ion feedback).

Pulse pile-up is monitored by a fast summing amplifier attached in parallel to the four shaping amplifiers. When a pulse is detected above a certain charge level, which may be set independently of the discriminator threshold described above, the pulse-pile-up rejection logic is enabled. If a second pulse arrives before the analog-to-digital conversions are completed, both events are assumed to be corrupted and are rejected. New pulses are "locked out" by the pulse-pile-up rejection logic until the shaping amplifiers have had time to return to their baseline level. If another pulse arrives before this occurs, the pulse lock-out time is reset. In this way "pile-up" of pulses separated by at least 50 ns can be detected. Since this is about 1% of the 4.5 μs needed to handle an event, pulse pile is effectively eliminated as a source of errors in position calculation.

The position of the electron impact on the anode is calculated from the digitized charges on the A, B and C electrodes. The digitizer electronics output a 16-bit address for each electron, 8-bits each in X and Y. This gives a detector spatial resolution of 256 x 256 pixels, where each pixel is approximately 300 μm square.

5.1. Capacitive coupling

Capacitive coupling between the discrete electrodes of the wedge-and-strip anode distorts the image. If a certain charge is deposited onto one electrode, charge will also be induced on the other electrodes, $\Delta Q = C\Delta V$. In an ideal preamp the input is a virtual ground so ΔV would be zero. Since the real amplifier has finite gain the input impedance is non-zero and the input signals are coupled. If Q_A, Q_B and Q_C are the incident charge distribution due to the anode geometry, the measured charge distribution will be

$$\begin{aligned} Q_a &= (1-\alpha-\gamma)Q_A + \gamma Q_B + \alpha Q_C \\ Q_b &= (1-\beta-\gamma)Q_B + \gamma Q_A + \beta Q_C \\ Q_c &= (1-\alpha-\beta)Q_C + \alpha Q_A + \beta Q_B \end{aligned} \tag{2}$$

where α, β and γ are the coupling constants between electrodes A—C, B—C and A—B, respectively.

Instead of the geometrical position (x,y) being calculated from the geometrical charge distribution Q_A, Q_B and Q_C, a distorted position

$$\begin{aligned} x' &= (1-2\alpha-\gamma)\,x + (\gamma-\alpha)\,y + \alpha \\ y' &= (1-2\beta-\gamma)\,y + (\gamma-\beta)\,x + \beta \end{aligned} \tag{3}$$

is calculated from the measured charge distribution Q_a, Q_b and Q_c. This coupling has two effects -- first the overall size of the image is reduced, since the degree of charge division $f_{\max} - f_{\min}$ is reduced, and second the image is distorted because of the coupling between x and y. This distortion corresponds to a compression of distances in the image along the $x = -y$ diagonal relative to distances along the $x = y$ diagonal.

For the wedge-and-strip anode $\alpha \approx \beta > \gamma$ since the A and B electrodes are separated by the C electrode. If an additional external capacitor connecting the A (wedge) and B (strip) electrodes is added to the anode to equalize the inter-electrode capacitances so $C_{AB} = C_{BC} = C_{AB}$, the coupling constants will be equal and the anode image will be undistorted, with

$$x'' = \epsilon\, x + x_o \quad \text{and} \quad y'' = \epsilon\, y + y_o \tag{4}$$

where $\epsilon = 1 - 3\alpha$ is a scale factor and (x,y) is the geometrical position

The rise time of a charge sensitive amplifier is[34]

$$\tau_{rise} = Z_{in} C_{in} = \frac{C_o\, C_{in}}{g_m\, C_f} \tag{5}$$

where Z_{in} is the amplifier input impedance, g_m is the amplifier transconductance gain, C_f is the feedback capacitance and C_o is the output capacitance. The feedback capacitance C_f determines the gain of the integrating preamp and g_m is a property of the amplifier. In our detector C_f = 40 pF, which gives a 40 mV output pulse for an input charge of 1.6 pC. The output capacitance C_o can be increased to "roll off" the pre-amp frequency response and decrease the noise bandwidth, however, this causes a proportional increase in the pre-amp input impedance and this in turn increases the capacitive coupling between the A, B and C electrodes, which degrades the anode performance.

The anode coupling constants were measured experimentally by connecting the anode to the pre-amplifier and driving one channel with a test pulse, then measuring the shaping amplifier output pulse heights. This gave $\alpha, \beta \approx = 0.18$ and $\gamma \approx 0.12$ with the maximum pre-amp band-width (with no external roll-off capacitance C_o for minimum Z_{in}).

The measured wedge-and-strip anode capacitances were $C_{AB} = 256$ pF and $C_{AC} = C_{BC} = 441$ pF for the anode alone. When the detector was installed in the vacuum chamber with magnetic and electrostatic shielding and the preamp cables were connected $C_{AB} = 545$ pF and $C_{AC} = C_{BC} = 721$ pF. After the inter-electrode capacitances were balanced $C_{AB} = C_{BC} = C_{CA} = 1010$ pF. This method of correcting the anode distortions increases the amplifier noise by $\sim 50\%$ and decreases the image size by $\sim 30\%$ for a further reduction in resolution.

There is an alternative solution to the anode distortion problem. For the case when $\alpha = \beta \neq \gamma$, which is a good approximation for the wedge-and-strip geometry, a new position calculation algorithm

$$x = k\,\frac{Q_b - fQ_c}{Q_a + Q_b + Q_c} + x_o \quad \text{and} \quad y = k\,\frac{Q_a - fQ_c}{Q_a + Q_b + Q_c} + y_o \tag{6}$$

may be used in place of the original position algorithm, where $f = \dfrac{\gamma - \alpha}{1 - 3\alpha}$ and Q_a, Q_b and Q_c are the experimentally measured charges. This algorithm gives the undistorted geometrical position directly in terms of the measured charges without the addition of external capacitors. With the modified algorithm the resolution is better by $\sim 50\%$ and the input capacitance is smaller.

The position calculation algorithm of Eq. 6 was implemented by the circuit shown in figure 4. Two 12 bit EPROM lookup tables were used to calculate the fC and $k/(A + B + C)$ terms. The digitizer produces analog outputs to drive a real-time oscilloscope display as well as the 16 bit address (8 bits each for x and y) of the electron event. The address data is analyzed by an 80386 PC computer system using a CAMAC histogramming memory module with 256x256 channels. This device adds one count to a

channel each time an address arrives and can run at 2 MHz.

6. Performance

The total counting rate of the channel plate chevron array is the main factor that limits the performance of the digital LEED detector. Electronic noise in the position calculation electronics reduces the detector spatial resolution and broadens spots but does not affect the measurement of LEED intensities. The detector resolution is more than adequate to determine integrated LEED beam intensities for ordered overlayers, and even less spatial resolution is required to measure diffuse LEED intensities from disordered adsorbates.

6.1. Count rates

In high count-rate applications a limit on the total count rate comes from the bias current flowing along the walls of the channels. Gain starts to drop significantly when the electron output current exceeds $\sim$ 20% of this bias current.[21] The bias current of our 75 mm channel plates is 30 μA, so the maximum linear pulse output is $\sim$ 1.5 nA/mm^2 or 230 Hz/mm^2 for 6.5 pC pulses. This limit corresponds to $\sim$ 1 MHz over the whole channel plate.

LEED measurements with channel plates can be a problem since most of the scattered electrons are concentrated into diffraction beams with intensities several orders of magnitude above the average. The RC time constant for an individual channel in the channel plate is $\sim$ 8 ms. When the effects of polarizing the adjacent channels are

considered, the effective recharge time is $\sim 5RC$ or 40 ms.[17,22] For a channel plate with 32 μm channel spacing there are about 1100 channels/mm^2. The time-constant estimate would imply a maximum local count-rate of $\sim$ 27 KHz/mm^2. Experimentally, the maximum linear count rate for a LEED diffraction beam lies between these limits. Under typical conditions the cross sectional area of beam on the detector is $\sim$ 1 mm^2 and the integrated count rate starts to saturate at around 5 kHz.

6.2. Statistics

In LEED experiments one tries to detect bright spots against a background of incoherently or thermally scattered electrons. Noise in the background usually dominates noise in the signal. If the integrated background intensity is a fraction β of the total intensity and a weak spot covering a percentage ΔA of the detector area has a fraction α of the total intensity, the number of counts needed to measure this intensity with a given signal to noise ratio is

$$N \geq (s/n)^2 \beta \Delta A / \alpha^2 \tag{7}$$

For typical values like $\beta = .75$, $\Delta A = 10^{-3}$, and $\alpha = 10^{-4}$, about 10^6 counts are required to determine the intensity with a signal to noise ratio of 5. This would take about 40 s at 50 kHz.

6.3. Position determination noise

Several studies have been made of the performance of wedge-and-strip anodes.[24,35,25,36,37,38] There are two main sources of noise in a position sensitive wedge-and-strip anode, partition noise and amplifier noise. Partition noise arises because of

statistical fluctuations in the division of electrons between the discrete electrodes. This can be significant since only 10^6 to 10^7 are incident on the anode. For our anode the worst case partition noise is $\sim 2/N^{1/2}$, so it should be possible to resolve over 1000 lines across the anode with 10^7 electrons per pulse.

The pre-amp noise, in terms of charge at the input, is

$$N_{noise} = \frac{C_{in} V_{in}}{e \tau^{1/2}} \tag{8}$$

where $C_{in} \sim 1000$ pF is the input capacitance due to the anode, $V_{in} \sim 1$ nV/ $\sqrt{\text{Hz}}$ is the amplifier voltage noise density referred to the input and $\tau \sim 50$ ns is the rise-time of the input charge pulse. This gives a noise of ~ 5 fC or $3 \cdot 10^4$ electrons. For our anode the partition noise is $\sim 2\ \Delta N/N$ or 0.6%, which corresponds to a resolution of about 150 lines at 10^7 electrons per pulse, or 700 lines for 6.5 pC pulses. Narrowing the preamp bandwidth to reduce amplifier noise does not help much since this increases the preamp input impedance and the capacitive coupling, which in turn reduces the charge division ratio and increases the noise.

6.4. Detector tests

The linearity and resolution of the LEED detector was tested by mounting an electron gun directly opposite the detector and placing a copper mask with a 5 mm grid of etched pinholes in front of the channel plates. The electron beam could be imaged over the entire detector with no apparent distortions at the outer edges of the channel plates and the linearity was quite good once the digitizer parameters were properly calibrated. The total dark count rate is less than 50 Hz or 10^{-3} Hz/pixel for pressures less than

$5 \cdot 10^{-10}$ torr. At higher pressures additional background counts are contributed by the ion pump.

7. Experimental results

7.1. Conventional I-V curves

The digital LEED detector has been used to obtain LEED intensity voltage (I-V) curves on the clean Pt(111) surface at normal incidence (figure 5). Intensity peaks for symmetrically equivalent beams agree in position and number. The absolute intensity levels differ because of the variation in electron impact angle relative to channel angle across the channel plate. The I-V curves obtained with the digital detector are similar to those obtained with conventional LEED detectors.[39]

7.2. Diffuse LEED data

The LEED detector has been used to record diffuse LEED patterns for molecular adsorbates without long-range order. When CO is adsorbed on Pt(111) at room temperature at coverages below 0.5 monolayer there is no long range order in the CO layer, which contributes diffuse LEED scattering in addition to the diffraction beams of the ordered substrate. Analysis of the diffuse intensities shows that CO is adsorbed in top and bridge sites. The adsorption geometries and the relative occupations of each site were determined.[11]

A study of the structure of disordered benzene adsorbed on the platinum (111) surface is now underway using the LEED system. Benzene produces ordered LEED patterns when coadsorbed with carbon monoxide on Pt(111). When benzene is adsorbed without CO, there is no long range order detectable by LEED.[40,41] Figure 6(a) shows the LEED pattern of a clean Pt(111) surface at 160 K recorded with a beam energy of 85eV. The retarding grids were set at 2 eV below the beam energy. Image data was accumulated for 300 s at a count rate of 7.94 kHz. The dark count rate was measured at 40 Hz just prior to data collection. The diffuse background is relatively featureless. The peak intensities of the Bragg beams are $\sim 10^3$ times larger than the average background intensity.

Figure 6(b) shows the pattern obtained from a surface covered with a single layer of disordered benzene molecules. This image was taken under the same beam conditions as figure 6(a). The benzene overlayer increased the reflection coefficient of the surface by $\sim$ 16% relative to clean Pt(111). The background has clearly increased and structure can be seen in the diffuse intensity. In order to eliminate the substrate contribution to the diffuse intensity, the clean surface LEED pattern is subtracted from the benzene covered pattern as shown in figure 6(c). The Bragg beams have been suppressed so the diffuse details are clear. It is clear that the diffuse features due to the overlayer reflect the symmetry of the system. Theoretical calculations have been made to determine the benzene adsorption geometry by fitting the distribution of diffuse electron scattering intensity.[42]

7.3. "Diffuse" I-V curves

An alternative method of analyzing diffuse LEED intensities by measuring "I-V" curves rather than spatial intensity distributions has recently been proposed by Heinz and collaborators.[43,44] In conventional LEED experiments on surfaces with long range order I-V spectra can be obtained by integrating the diffracted electron intensities in small areas or "windows" around each LEED beam at successive energies. In most LEED instruments the diffracted beams move across the detector as the incident electron energy changes, and the beams must be tracked to generate I-V curves.

The pattern of LEED beams or spots depends on the size and shape of the surface unit cell, and each LEED beam corresponds to a particular value of momentum transfer parallel to the surface ($\Delta \mathbf{k}_{||}$). Although the long range order of surface unit cells determines the number and location of LEED beams in terms of $\Delta \mathbf{k}_{||}$, the actual intensity (I-V) variations in a given beam are determined by the local structure of the surface, since the mean free path for electrons in solids at the energies used for LEED is on the order of a few Angstroms. This means that the diffuse LEED intensity variations for a given value of $\Delta \mathbf{k}_{||}$ due to an adsorbate with a well-defined local adsorption geometry but without long range order should be the same as that of an (hypothetical) I-V curve at the same value $\Delta \mathbf{k}_{||}$ from an ordered overlayer with the same local adsorption geometry. Experimental results of Heinz *et al.* demonstrate this equivalence,[43] which is implicit in the "beam set neglect" formalism of Van Hove *et al.*[5] which has been applied to diffuse LEED calculations.[6]

Diffuse "I-V" curves have been measured experimentally for adsorbates without long range order. In a fashion similar to conventional I-V measurements, diffuse

intensities can be measured as function of energy by integrating the diffuse intensity within a window at constant $\Delta\mathbf{k}_{||}$. As the incident electron energy changes, the window has to be moved in order to keep $\Delta\mathbf{k}_{||}$ constant, and a window size correction is needed to keep the integration area constant in $\mathbf{k}_{||}$-space. Since there is no diffraction spot to track, the detector coordinates for the desired value of $\Delta\mathbf{k}_{||}$ must be determined by an alternate method. One possibility is to use LEED beams from the ordered substrate as reference points, another is to record a track for an overlayer LEED beam from a separate calibration run on an ordered superstructure.[43] Experimental measurements of diffuse I-V curves are more difficult than for conventional I-V curves since the intensity of a normal diffracted beam is $\sim N^2$ while the intensity of a diffuse "beam" is only $\sim N$ where N is the number of unit cells contributing to the beam. The digital LEED detector is well suited to this task because of its sensitivity and large dynamic range.

We have measured diffuse I-V curves from two different disordered molecular overlayers on Pt(111), benzene adsorbed at room temperature, and water adsorbed at $\sim$ 80 K. We recorded diffuse "I-V" curves on a 4x4 grid of $\Delta\mathbf{k}_{||}$ values within the Pt(111) unit cell. In this way we simulate a ordered p(4x4) overlayer and collect all the information available from the diffuse LEED intensities -- a finer grid would produce redundant data.[44] The c(4x2)-CO/Pt(111) LEED pattern[39] was used to record the window tracking, whereby positions of missing spots were interpolated. A selection of spectra for both adsorbate systems is shown in figure 7. Theoretical calculations to obtain the structure of the adsorbed molecules including modifications of the substrate geometry (local reconstructions) are now underway for benzene[45] and water.[46]

Acknowledgement

Prof. D. A. Shirley provided enthusiastic support and encouragement for the development of the digital LEED system. His students Steve Robey provided practical advice and a UV source for anode fabrication, and John Barton offered helpful information on detector and anode algorithms. We also acknowledge useful discussions with O.W.H. Siegmund. This work was supported by the Director, Office of Energy Research, Office of Basic Energy Sciences, Materials Science Division, of the U.S. Department of Energy under Contract No. DE-AC03-76SF00098. One of us (U.S.) gratefully acknowledges financial support by the Deutsche Forschungsgemeinschaft (DFG).

References

1. J. M. MacLaren, J. B. Pendry, P. J. Rous, D. K. Saldin, G. A. Somorjai, M. A. Van Hove, and D. D. Vvedensky, *Surface Crystallographic Information Service,* Reidel, Dordrecht, 1987.

2. M. A. Van Hove, S. W. Wang, D. F. Ogletree, and G. A. Somorjai, *Advances in Quantum Chemistry*, vol. 20, p. 1, 1989.

3. K. Heinz, *Progress in Surface Science*, vol. 27, p. 239, 1988.

4. J. B. Pendry and D. K. Saldin, *Surface Science*, vol. 145, p. 33, 1984.

5. M. A. Van Hove, R. F. Lin, and G. A. Somorjai, *Physical Review Letters*, vol. 51, p. 778, 1983.

6. D. K. Saldin, J. B. Pendry, M. A. Van Hove, and G. A. Somorjai, *Physical Review B*, vol. 31, p. 1216, 1985.

7. K. Heinz, D. K. Saldin, and J. B. Pendry, *Physical Review Letters*, vol. 55, p. 2312, 1985.

8. P. R. Rous, J. B. Pendry, D. K. Saldin, K. Heinz, K. Müller, and N. Bickel, *Physical Review Letters*, vol. 57, p. 2951, 1986.

9. U. Starke, P. de Andres, D. K. Saldin, K. Heinz, and J. B. Pendry, *Physical Review B*, vol. 38, p. 12277, 1988.

10. U. Starke, W. Oed, P. Bayer, F. Bothe, G. Fürst, P. L. de Andres, K. Heinz, and J. B. Pendry, in *The Structure of Surfaces III*, ed. S. Y. Tong, M. A. Van Hove, X. Xide and K. Takayangi, Springer Verlag, Berlin, 1991.

11. G. S. Blackman, M.-L. Xu, D. F. Ogletree, M. A. Van Hove, and G. A. Somorjai, *Physical Review Letters*, vol. 61, p. 2352, 1988.

12. P. Piercy, P. A. Heimann, G. Michalk, and D. Menzel, *Surface Science*, vol. 219, p. 189, 1989.

13. D. F. Ogletree, G. A. Somorjai, and J. E. Katz, *Review of Scientific Instruments*, vol. 57, p. 3012, 1986.

14. P. Heilmann, E. Lang, K. Heinz, and K. Müller, in *Determination of Surface Structure by LEED*, ed. P. M. Marcus and F. Jona, p. 463, Plenum Press, New York, 1984.

15. Albert Rose and Paul K. Weimer, "Special Issue on the Physics of Imaging," *Physics Today*, vol. 42, p. 24, September 1989.

16. U. Starke, P. Bayer, H. Hloch, and K. Heinz, *Surface Science*, vol. 126, p. 325, 1986.

17. J. L. Wiza, *Nuclear Instruments and Methods*, vol. 162, p. 587, 1979.

18. Physical Electronics, Inc., LEED model 10-120, Eden Prairie, MN.

19. J. G. Timothy, *Review of Scientific Instruments*, vol. 52, p. 1131, 1981.

20. G. W. Fraser, J. F. Pearson, G. C. Smith, M. Lewis, and M. A. Barstow, *IEEE Transactions on Nuclear Science*, vol. NS-30, p. 455, 1983.

21. G. W. Fraser, *Nuclear Instruments and Methods*, vol. 221, p. 115, 1984.

22. E. Gatti, K. Oba, and P. Rehak, *IEEE Transactions on Nuclear Science*, vol. NS-30, p. 461, 1983.

23. Cliftronics, Inc., Model CE406, Clifton, NJ 07013.

24. C. Martin, P. Jelinsky, M. Lampton, R. F. Malina, and H. O. Anger, *Review of Scientific Instruments*, vol. 52, p. 1067, 1981.

25. O. H. W. Siegmund, R. F. Malina, K. Cobern, and D. Werthimer, *IEEE Transactions on Nuclear Science*, vol. NS-31, p. 776, 1984.

26. L. J. Richter and W. Ho, *Review of Scientific Instruments*, vol. 57, p. 1469, 1986.

27. P. C. Stair, *Review of Scientific Instruments*, vol. 51, p. 132, 1980.

28. E. G. McRae, R. A. Malic, and D. A. Kapilow, *Review of Scientific Instruments*, vol. 56, p. 2077, 1985.

29. J. G. Timothy, *IEEE Transactions on Nuclear Science*, vol. NS-32, p. 427, 1985.

30. M. Lampton and F. Paresce, *Review of Scientific Instruments*, vol. 45, p. 1098, 1974.

31. M. Lampton and C. W. Carlson, *Review of Scientific Instruments*, vol. 50, p. 1093, 1979.

32. Surface Science Laboratories, Palo Alto, CA.

33. H. O. Anger, *U.S. Patent 3,209,201*, 1965.

34. V. Radeka, *IEEE Transactions on Nuclear Science*, vol. 21, p. 51, 1974.

35. O. W. H. Siegmund, S. Clotheir, J. Thornton, J. Leman, R. Harper, I. M. Mason, and J. L. Culhane, *IEEE Transactions on Nuclear Science*, vol. NS-30, p. 503, 1983.

36. J. R. Arlington-Smith, I. M. Mason, H. E. Schwartz, and J. L. Culhane, *IEEE Transactions on Nuclear Science*, vol. NS-32, p. 119, 1985.

37. H. E. Schwartz and J. S. Lapington, *IEEE Transactions on Nuclear Science*, vol. NS-32, p. 433, 1985.

38. O. W. H. Siegmund, M. Lampton, J. Bixler, S. Bowyer, and R. F. Malina, to be published.

39. D. F. Ogletree, M. A. Van Hove, and G. A. Somorjai, *Surface Science*, vol. 173, p. 351, 1986.

40. D. F. Ogletree, M. A. Van Hove, and G. A. Somorjai, *Surface Science*, vol. 183, p. 1, 1987.

41. M. A. Van Hove, R.-F. Lin, G. S. Blackman, C. M. Mate, D. F. Ogletree, and G. A. Somorjai, *Journal of Vacuum Science and Technology A*, vol. 5, p. 692, 1987.

42. A. Wander, G. Held, R. Q. Hwang, G. S. Blackman, M.-L. Xu, P. L. de Andres, M. A. Van Hove, and G. A. Somorjai, *Surface Science*, (in press).

43. K. Heinz, U. Starke, and F. Bothe, *Surface Science Letters*, vol. 243, p. L70, 1991.

44. K. Heinz, U. Starke, M. A. Van Hove, and G. A. Somorjai, *Surface Science Letters*, (to be published).

45. U. Starke, A. Wander, G. Held, M. A. Van Hove, and G. A. Somorjai, (to be published).

46. U. Starke, N. Materer, A. Wander, K. Heinz, M. A. Van Hove, and G. A. Somorjai, (to be published).

Figure Captions

1) Schematic of the LEED detector showing the electron optics and a block diagram of the counting electronics and data system.

2) The "Wedge and Strip" anode and analog amplifier circuits. A schematic of a few periods of the wedge and strip anode is shown at left. The X coordinate is given by $\frac{Q_B}{Q_A + Q_B + Q_C}$ and the Y coordinate by $\frac{Q_A}{Q_A + Q_B + Q_C}$. The output of the charge sensitive preamps, connected to the three electrodes, consists of sharp steps for each charge pulse on a slowly decaying background. These signals go to integrating shaping amplifiers which produce smooth shaped pulses whose height is proportional to the charge deposited on the electrodes. Another circuit detects pulse pile up.

3) The position sensitive "wedge and strip" anode design used for the digital LEED detector. A is the wedge electrode and B is the strip electrode. The two sections of the C electrode fill the space between the other electrodes. The hole at the center is for the LEED electron gun.

4) The digital part of the position calculation circuit. The division operations are done by EPROM look-up tables for maximum speed.The values in these tables depend on the parameters of the anode.

5) LEED I-V curves for the clean Pt(111) surface recorded at normal incidence at room temperature using the digital LEED detector. Part (a) shows the (1,0) diffraction beam and the two other symmetrically equivalent beams, and and part (b) shows the (1,1) beam and the four other symmetrically equivalent beams. There is good agreement in peak positions and relative intensities between the beams and with Pt(111) I-V curves recorded with conventional LEED systems.

6) Digital LEED images of the Pt(111) surface at 85 eV and 160 K before and after benzene adsorption. The roughness at the upper left part of the outside diameter of the images results from a slight asymmetry in the energy retarding grids. The feature near the lower right edge of the inside diameter of the image is an artifact related to the placement of the electron gun beam tube and shield.

(a) Clean Pt(111)

(b) Pt(111) after benzene adsorption

(c) Difference image (b) - (a) after suppressing the diffraction beams

7) Diffuse intensity versus energy (I-V) spectra for disordered molecular adsorbates. Four spectra are shown for each system recorded at $\Delta\mathbf{k}_{||}$ positions where the overlayer beams of a p(4x4) superstructure would appear. (The baselines of the spectra are offset for clarity.)

(a) Diffuse I-V curves for disordered H_2O adsorbed on Pt(111) at $\sim$ 80 K. Adsorbed water is very sensitive to electron beam damage and can only be studied with a low current LEED instrument.

(b) Diffuse I-V curves for disordered benzene adsorbed on Pt(111). The low energy part of the (1/4,1/4) spectrum is plotted on a reduced scale due to its relatively high intensity.

Digital LEED Detector

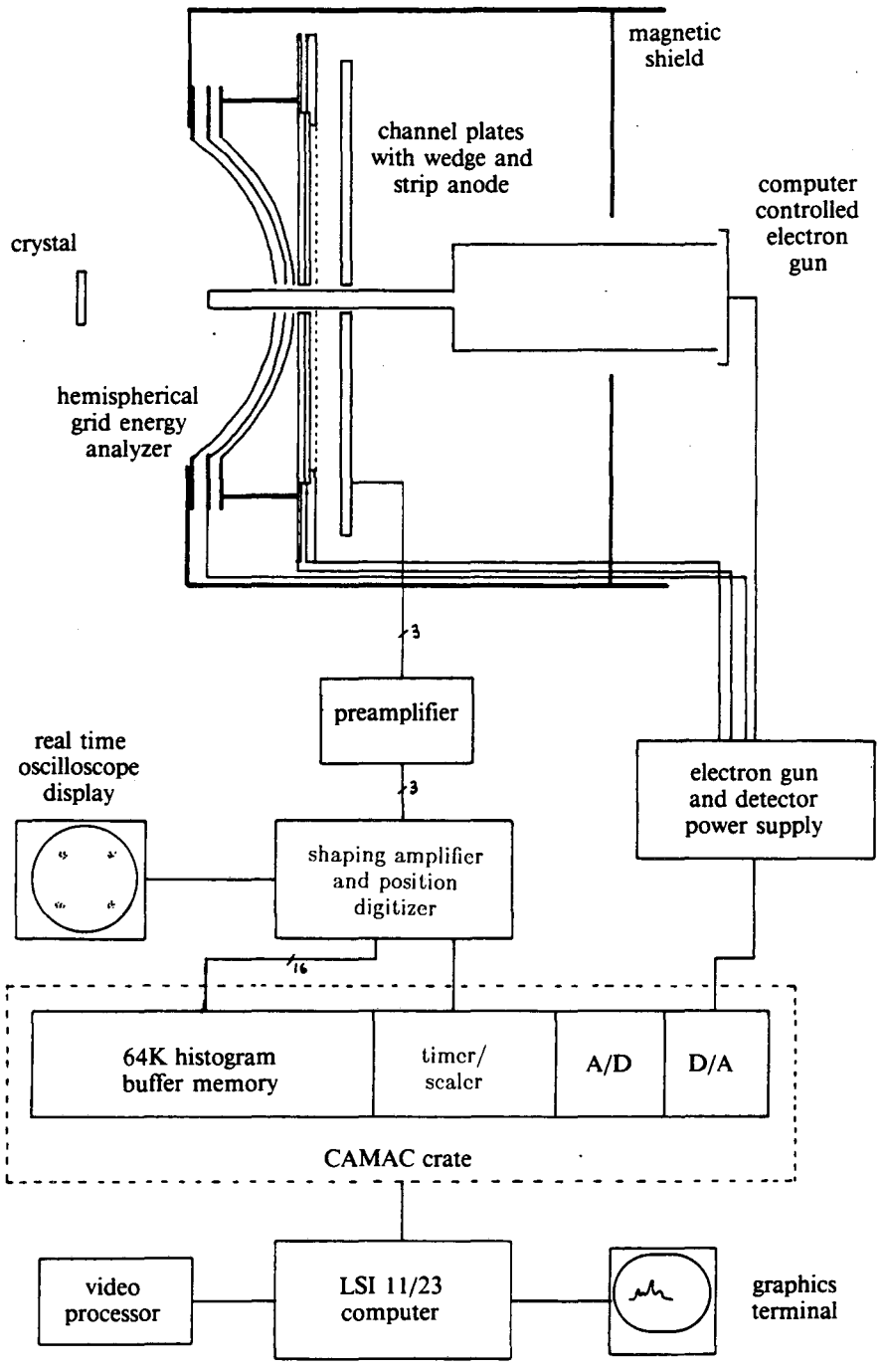

XBL 8512-5024

Figure 1

Position Sensitive Anode and Amplifier Circuit

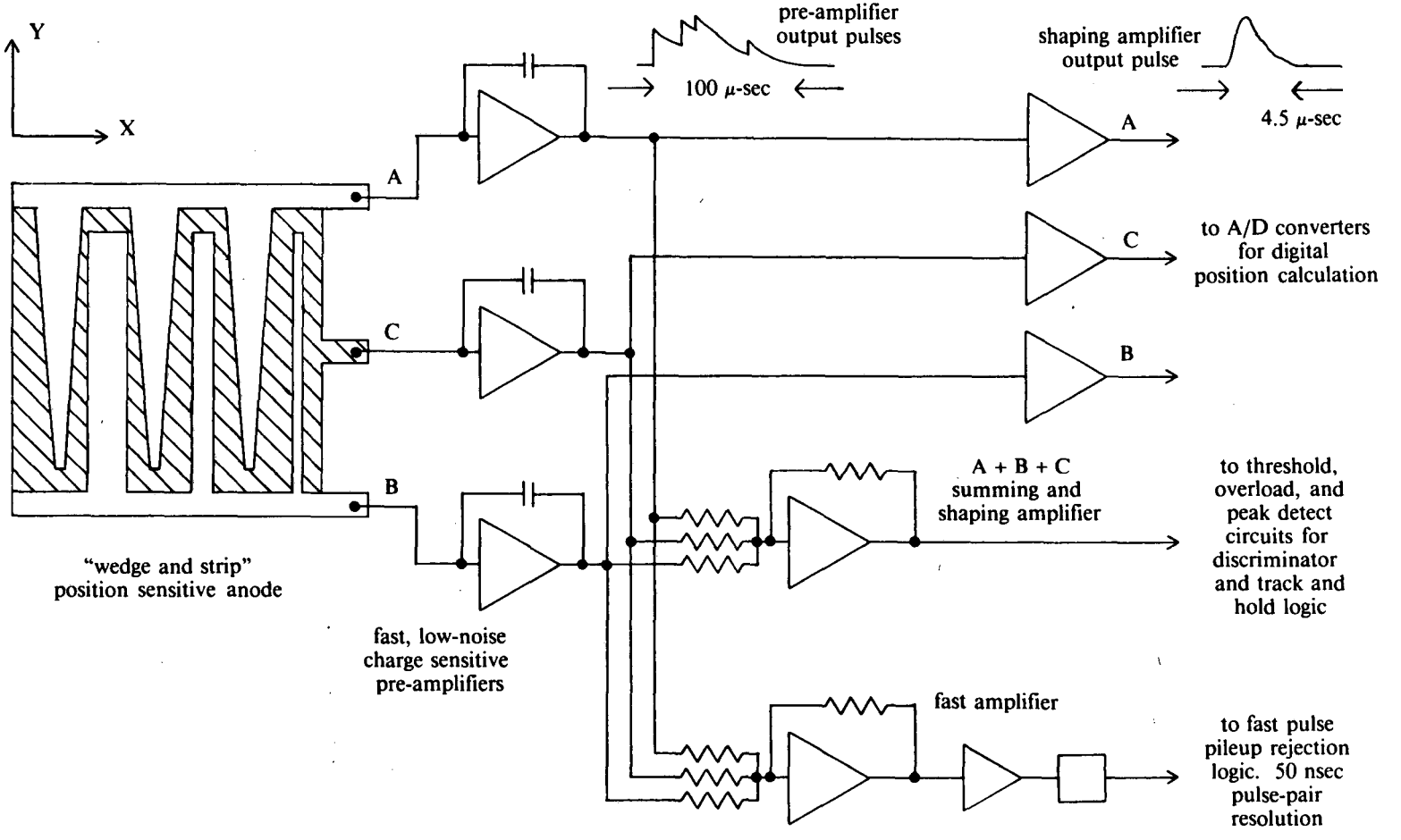

XBL 8512-5026

Figure 2

Wedge and Strip Anode

(actual size)

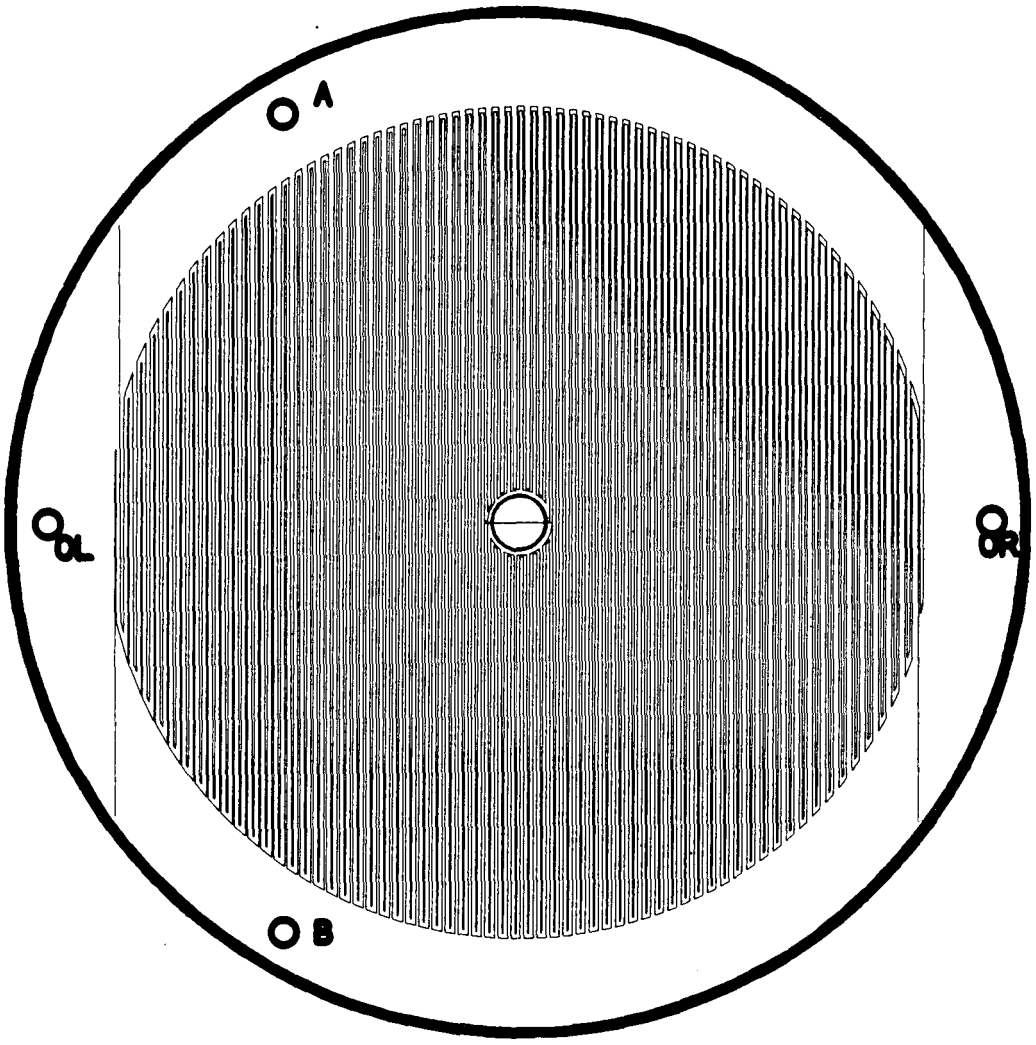

XBL 879-3865

Figure 3

LEED Digital Position Calculation Circuit

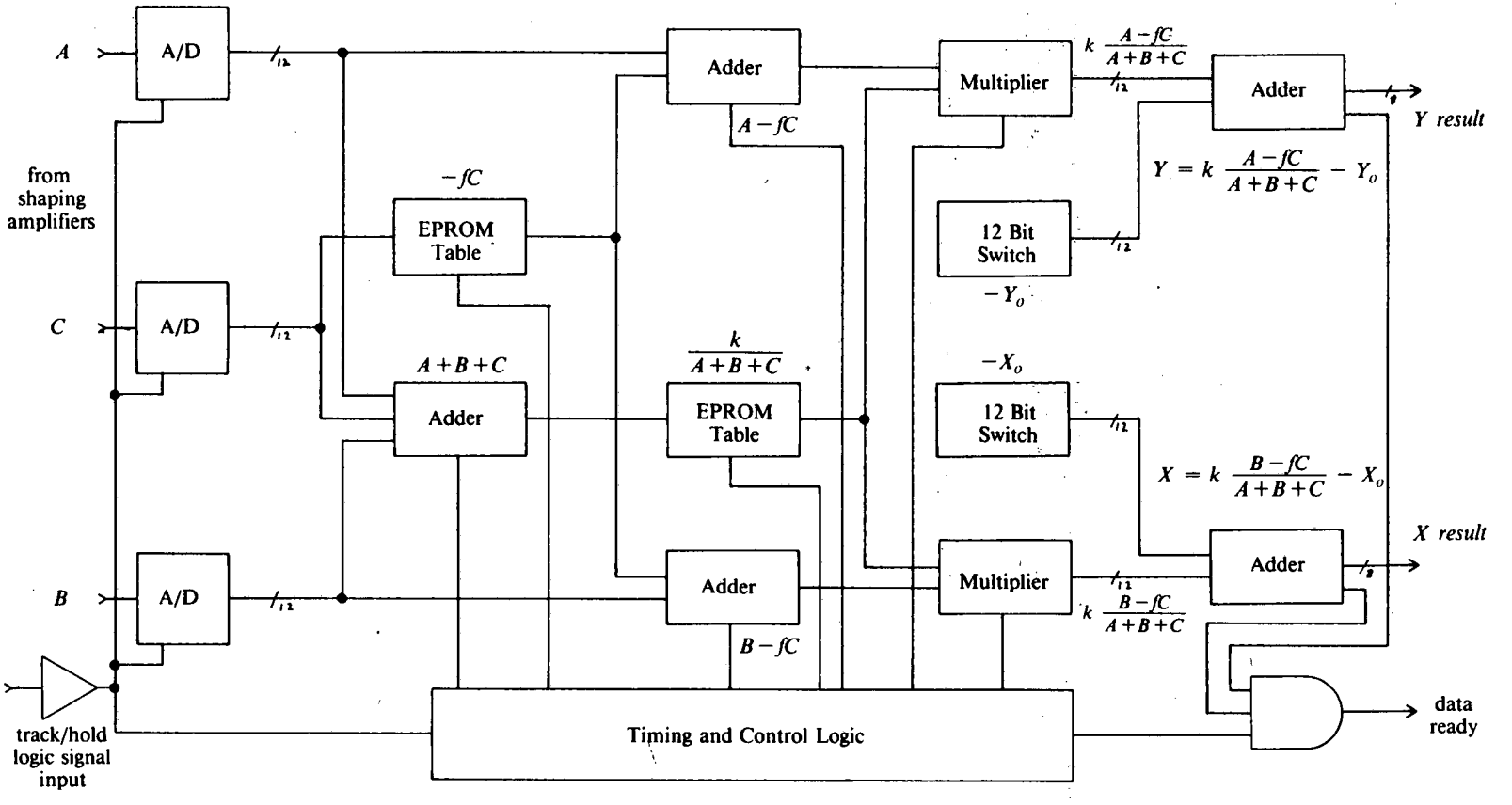

XBL 8512-5025

Figure 4

a)

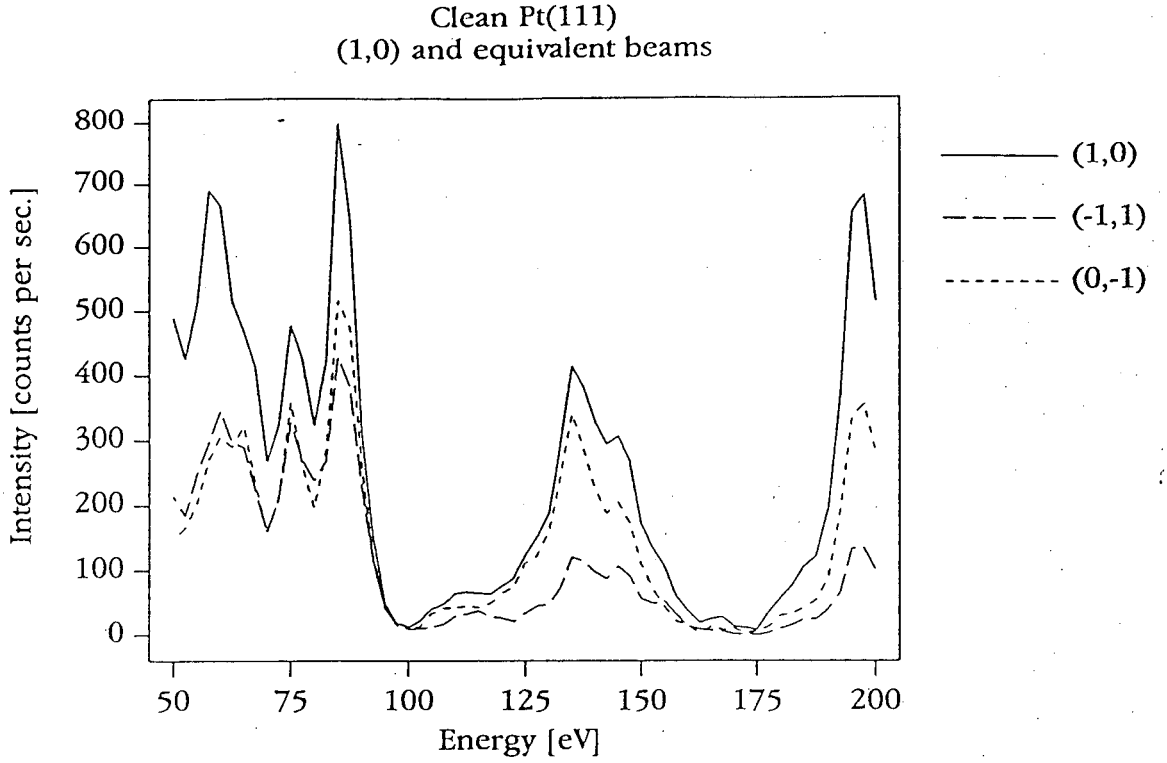
Clean Pt(111)
(1,0) and equivalent beams
Intensity [counts per sec.]
800
700
600
500
400
300
200
100
0
50
75
100
125
150
175
200
Energy [eV]
(1,0)
(-1,1)
(0,-1)

b)

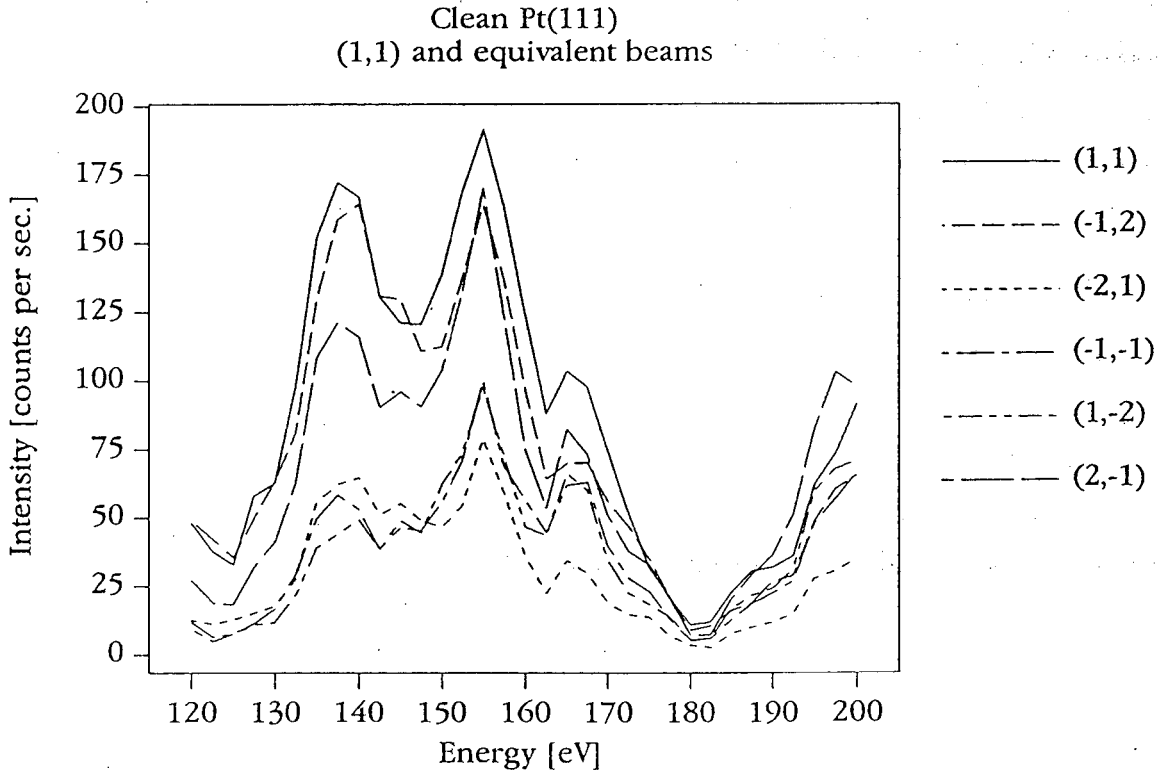
Clean Pt(111)
(1,1) and equivalent beams
Intensity [counts per sec.]
200
175
150
125
100
75
50
25
0
120
130
140
150
160
170
180
190
200
Energy [eV]
(1,1)
(-1,2)
(-2,1)
(-1,-1)
(1,-2)
(2,-1)

Figure 5

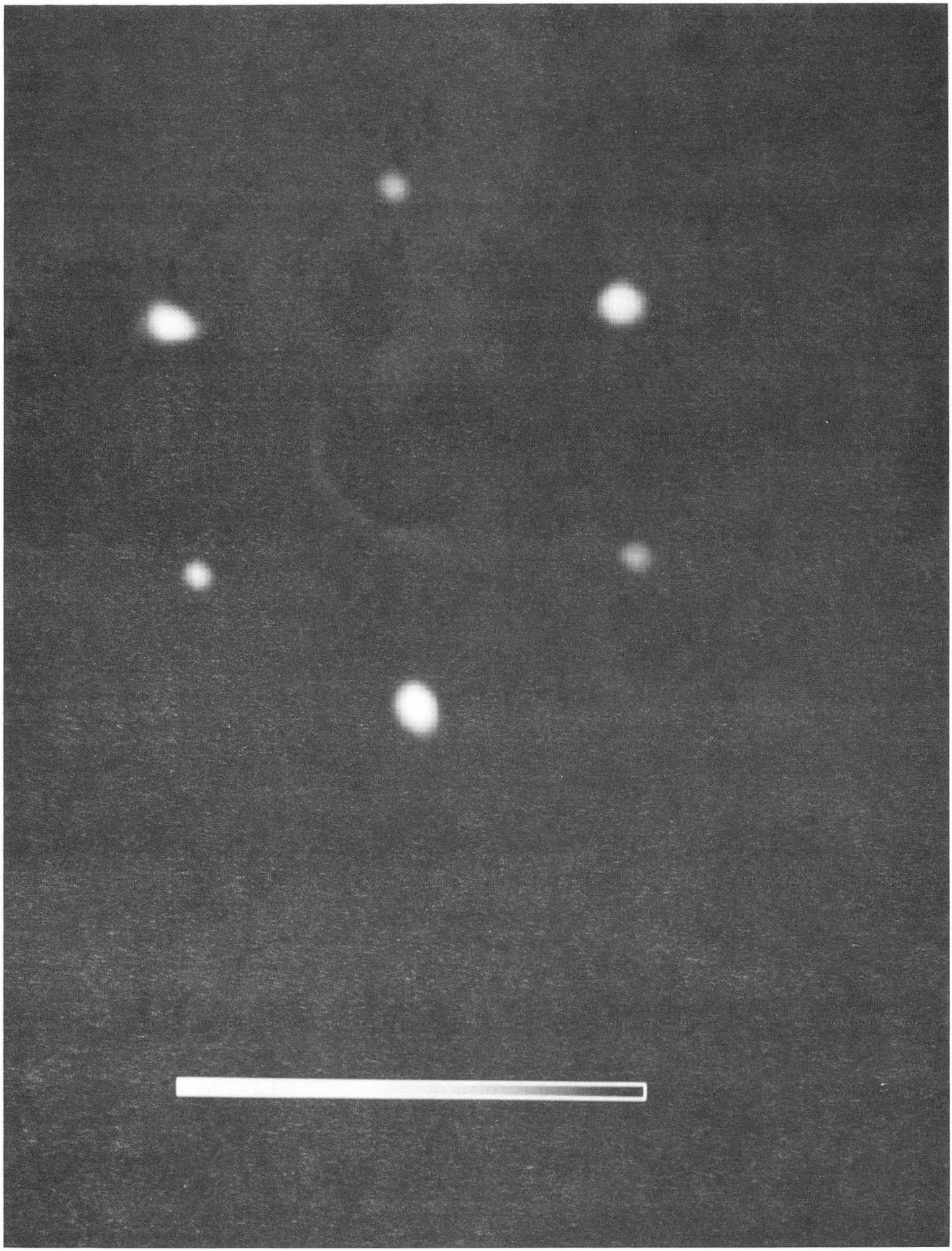

CBB 905-3570

Figure 6a

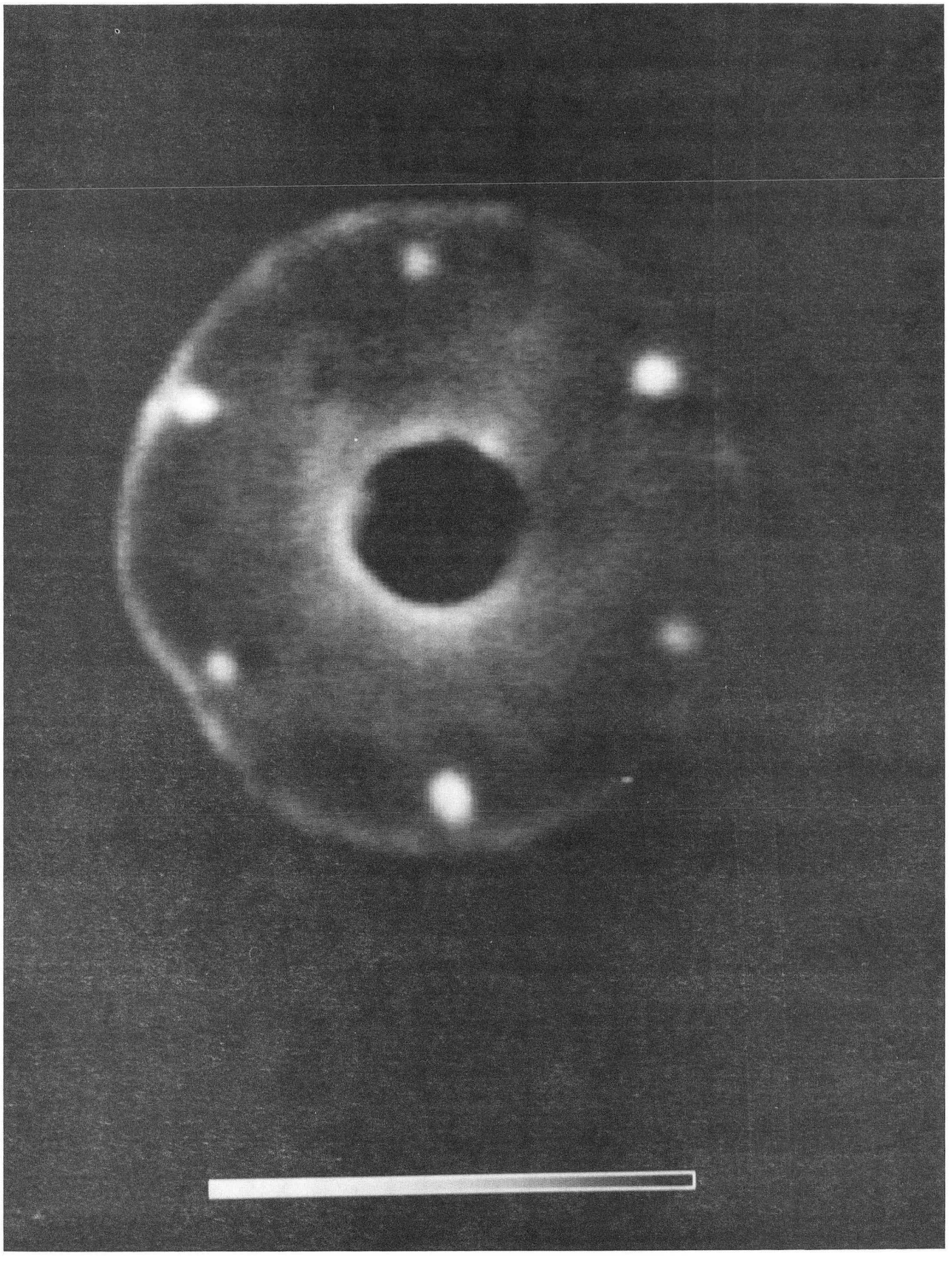

CBB 905-3584

Figure 6b

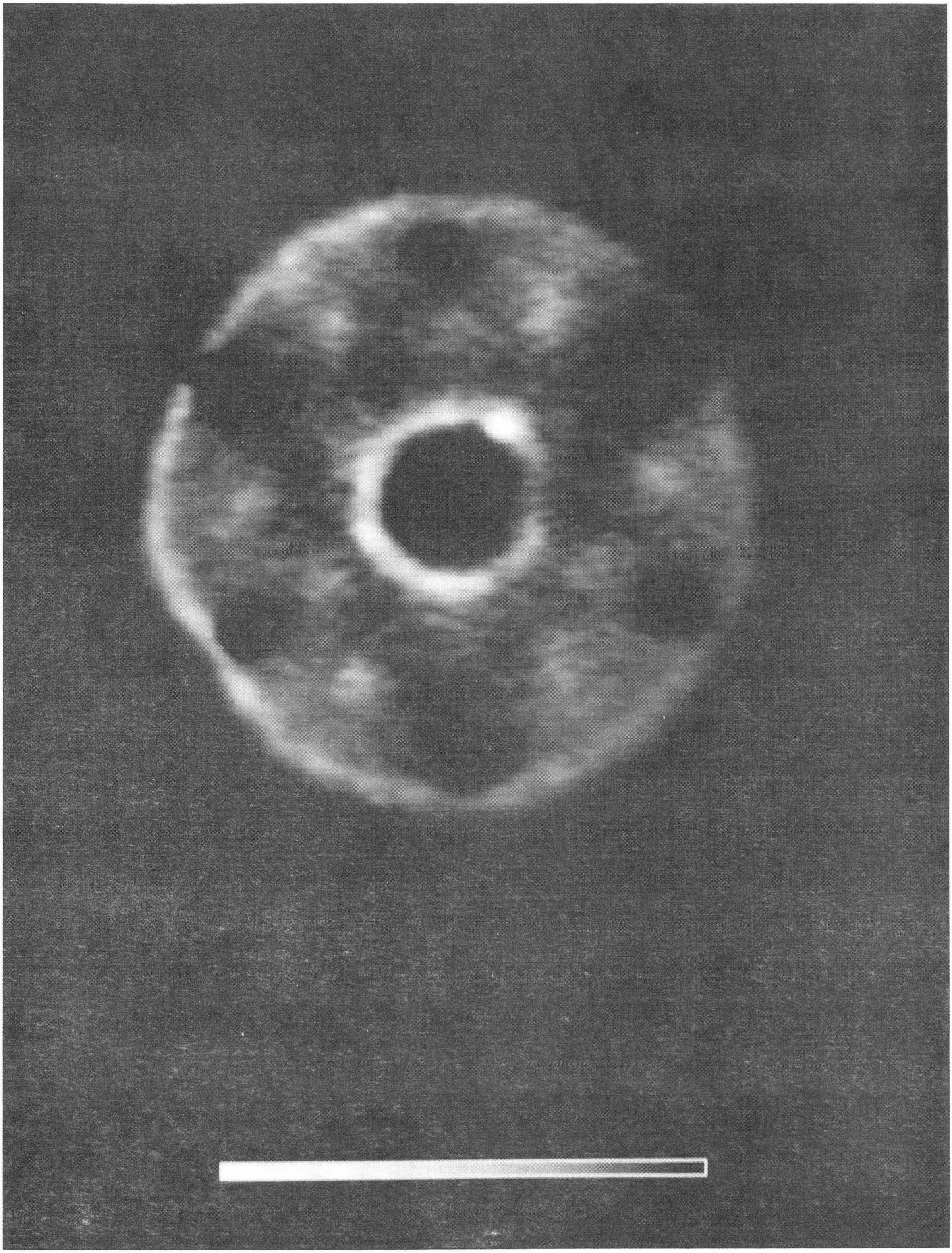

CBB 905-3580

Figure 6c

a)

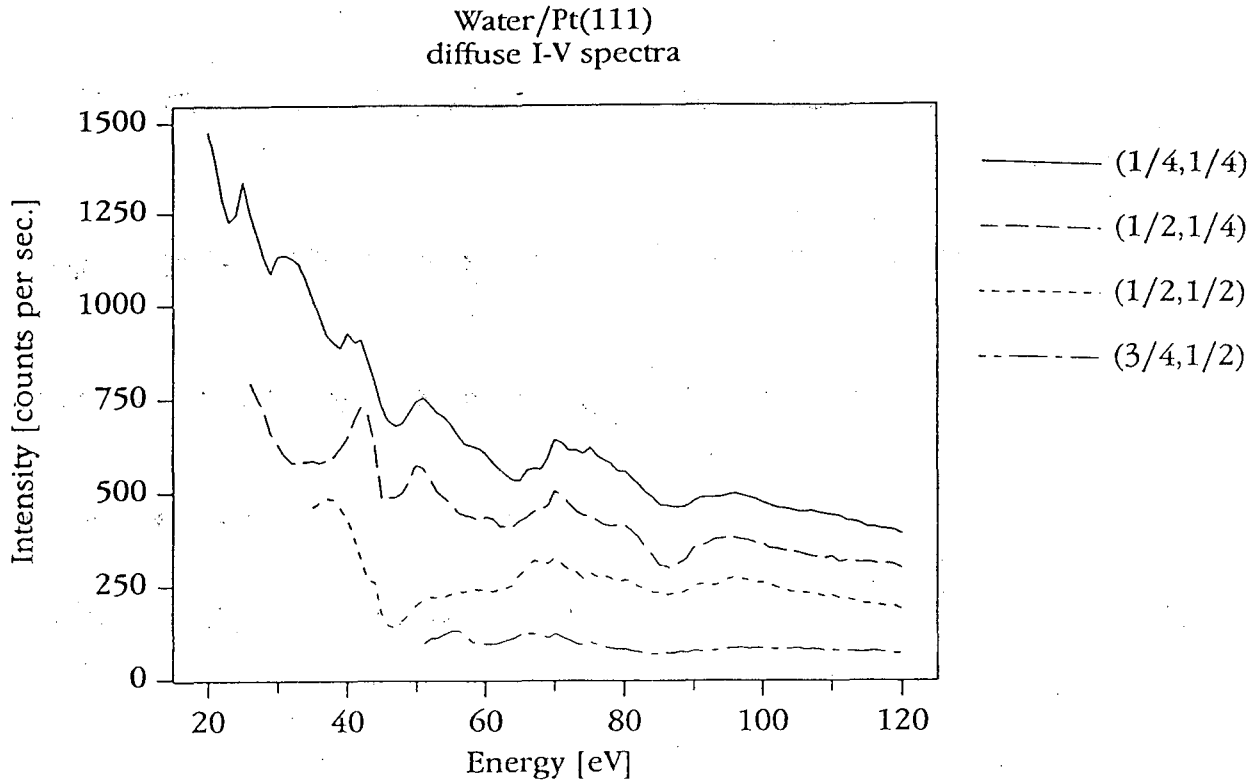
Water/Pt(111)
diffuse I-V spectra
Intensity [counts per sec.]
1500
1250
1000
750
500
250
0
20
40
60
80
100
120
Energy [eV]
(1/4,1/4)
(1/2,1/4)
(1/2,1/2)
(3/4,1/2)

b)

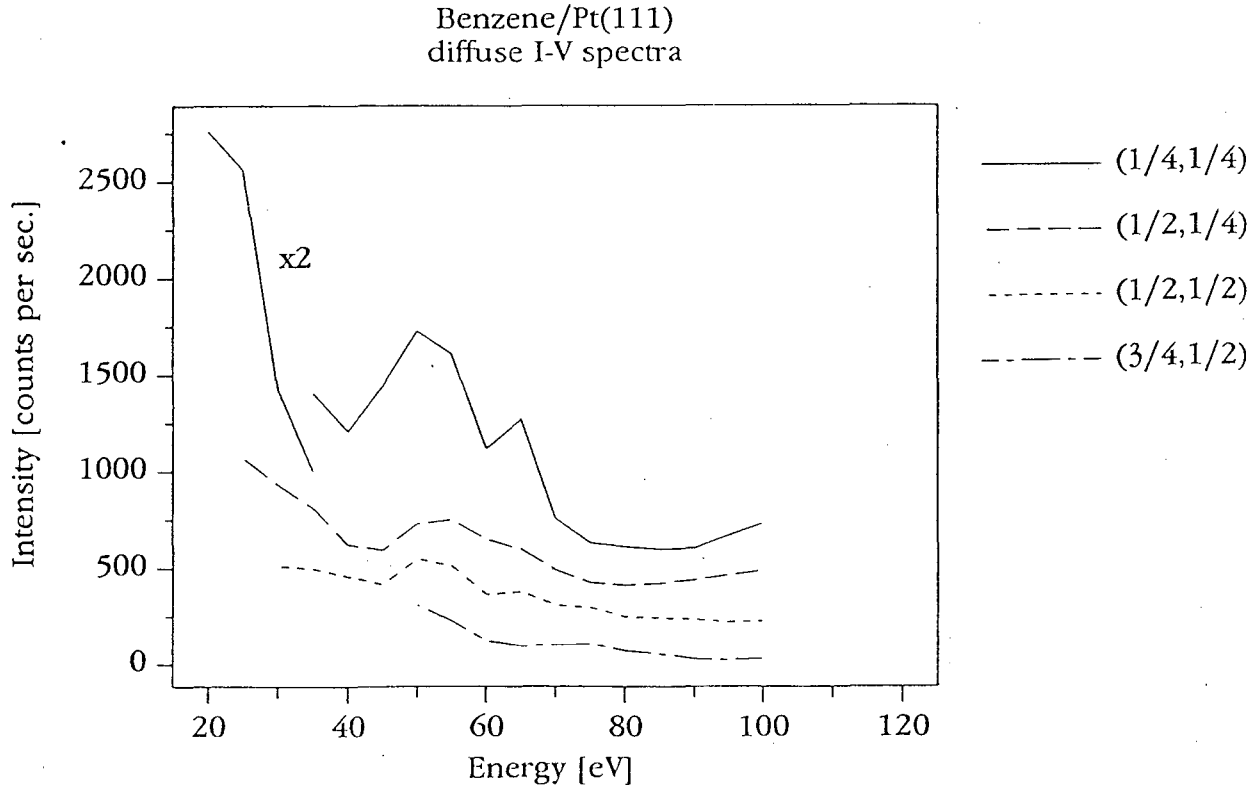
Benzene/Pt(111)
diffuse I-V spectra
Intensity [counts per sec.]
2500
2000
1500
1000
500
0
x2
20
40
60
80
100
120
Energy [eV]
(1/4,1/4)
(1/2,1/4)
(1/2,1/2)
(3/4,1/2)

Figure 7

FIGURES

1) XBL 8512-5024 LEED detector block diagram

2) XBL 8512-5026 LEED anode/preamp block diagram

3) XBL 879-3865 LEED anode mask

4) XBL 8512-5025 Digitizer block diagram

5) XBL ..., Pt(111) I-V curves

6a) CBB 905-3570 Pt(111) at 85 eV LEED image

6b) CBB 905-3584 Pt(111) and diffuse benzene LEED image

6c) CBB 905-3580 Difference image

7) XBL... diffuse I-V curves

LAWRENCE BERKELEY LABORATORY
CENTER FOR ADVANCED MATERIALS
1 CYCLOTRON ROAD
BERKELEY, CALIFORNIA 94720